Article

Controlled Synthesis of Nickel Phosphides in Hollow N, P Co-Doped Carbon: In Situ Transition to (Oxy)hydroxide Phases During Oxygen Evolution Reaction

David Ríos-Ruiz [1], Pablo Arévalo-Cid [1,*], Jesús Cebollada [1], Verónica Celorrio [2], Miran Čeh [3], Sandra Drev [4] and María Victoria Martínez-Huerta [1,*]

[1] Instituto de Catálisis y Petroleoquímica (CSIC), Marie Curie 2, 28049 Madrid, Spain; david.rios@csic.es (D.R.-R.); jesus.cebollada@csic.es (J.C.)

[2] Diamond Light Source Ltd., Harwell Science & Innovation Campus, Didcot OX11 0DE, UK; veronica.celorrio@diamond.ac.uk

[3] Department for Nanostructured Materials, Jožef Stefan Institute, Jamova 39, 1000 Ljubljana, Slovenia; miran.ceh@ijs.si

[4] Center for Electron Microscopy and Microanalysis, Jožef Stefan Institute, Jamova 39, 1000 Ljubljana, Slovenia; sandra.drev@ijs.si

* Correspondence: pablo.arevalo@csic.es (P.A.-C.); mmartinez@icp.csic.es (M.V.M.-H.)

Abstract: Developing sustainable and efficient electrocatalysts for the oxygen evolution reaction (OER) is crucial for advancing energy storage technologies. This study explored the dual role of phosphorus as a dopant in carbon matrices and a key component in nickel phosphides (Ni_2P and $Ni_{12}P_5$), synthesized using dopamine (PDA) and ammonium phosphate as eco-friendly precursors. The phase formation of nickel phosphides was found to be highly dependent on the P/PDA ratio (0.15, 0.3, 0.6, and 0.9), allowing for the selective synthesis of Ni_2P or $Ni_{12}P_5$. Operando Raman spectroscopy revealed that both phases undergo surface transformation into nickel (oxy)hydroxide species under OER conditions, yet Ni_2P-based catalysts demonstrated superior activity and long-term stability. This enhancement is attributed to efficient electron transfer at the dynamic Ni_2P/NiOOH interface. Additionally, hollow nanostructures formed at intermediate P/PDA ratios (≤ 0.3) via the Kirkendall effect and Ostwald ripening contributed to an increased specific surface area and micropore volume, further improving the catalytic performance. Electrochemical impedance spectroscopy confirmed reduced interfacial resistance and enhanced charge transport. These findings offer new insights into the rational design of high-performance electrocatalysts and propose a green, tunable synthesis approach for advanced energy conversion applications.

Keywords: electrocatalyst; nickel phosphide; hollow nanostructures; co-doped carbon; solvothermal method; polydopamine; oxygen evolution reaction

1. Introduction

The oxygen evolution reaction (OER) plays a key role as the anodic process in various energy storage technologies, such as CO_2 electrolyzers, ammonia synthesis, and water splitting. It significantly influences the overall energy efficiency of these electrochemical devices, as its inherently slow kinetics result in a significant overpotential, necessitating the use of highly efficient catalysts. The OER involves a complex four-electron transfer process, which includes the breaking of O-H bonds and the formation of O-O bonds. These steps

introduce substantial kinetic energy barriers, requiring a potential considerably higher than the thermodynamic minimum to drive the reaction effectively [1,2].

Up to now, the most widely used OER catalysts have been ruthenium and iridium oxides. Due to the high cost and earthly shortage of these metals, the extensive implementation of this technology requires the development of more affordable catalysts based on abundant elements [2–4]. Over the past decade, many improvements have been made to non-precious-metal-based catalysis. For instance, oxides and hydroxides derived from late 3d transition metals such as Ni, Fe, Co, and Mn are recognized as highly active catalysts for the oxygen evolution reaction in alkaline and neutral pH environments [5–7].

In recent years, electrocatalysts based on transition metal phosphides (TMPs) have garnered considerable interest owing to their versatile active sites, adjustable structures and compositions, and distinctive physicochemical properties [8,9]. Fe, Co, and Ni phosphides with various compositions have proven to be effective catalysts for water splitting [10–12]. The superior activity of the metal phosphides could be due to the efficient carrier transfer via a phosphide-(oxy)hydroxide interface [13]. Phosphide materials are good electrical conductors that remain at the core, while an (oxy)hydroxide overlayer forms on their surfaces during catalytic transformation. This interface helps provide better carrier transport from the core phosphide to the (oxy)hydroxide layer. Among them, nickel phosphides possess unique structural and electronic characteristics conducive to electrocatalytic activity. Nickel phosphides exist in different phases, such as metal-rich nickel phosphides (Ni_2P, $Ni_{12}P_5$, Ni_3P, Ni_7P_3, Ni_5P_4) and phosphorus-rich nickel phosphides (NiP_2, NiP_3) [14]. Furthermore, different morphologies of nickel phosphides, such as nanoplates, rods, spheres, wires, or amorphous nanostructures, can display favorable characteristics for electrocatalysis. However, these materials are usually synthesized using non-sustainable methods, such as the hot trioctylphosphine (TOP) route [15,16], chemical vapor deposition (CVD) techniques [11,17], or low-temperature organic solvent phosphidation [10].

Carbon materials are often employed as support for transition metal phosphides. The carbon matrices facilitate efficient electron transfer through the conductive carbon network and provide a high specific surface area, enabling the exposure of a more significant number of catalytic active sites. As research in this field has advanced, it has become evident that integrating carbon materials doped with heteroatoms, such as N, P, or S, with TMPs can produce synergistic effects in electrocatalysis [8,18–21]. A common challenge with nanoscale catalysts is their high surface energy, making them prone to aggregation during synthesis or electrochemical testing and reducing active site availability. However, the carbon matrix can effectively mitigate this issue by confining and stabilizing the nanoparticles, thereby preventing their aggregation.

As a dopant, phosphorus modifies the electronic structure and surface properties of carbon materials. Phosphorus doping introduces defects into the carbon lattice, improving its conductivity and optimizing the adsorption energies of reaction intermediates. These modifications facilitate efficient electron transfer and promote electrocatalytic reaction kinetics [22,23]. Moreover, phosphorus has been described as a catalytic activity booster when co-doped with carbonous materials and nitrogen [24–26]. The activity of these co-doped carbon materials is susceptible to the synthesis conditions (temperature, heat treatment, precursors), as these factors influence the physico-chemical features of the electrocatalysts and, in turn, the electroactivity.

In this work, we investigated a synthesis method capable of co-doping carbon with nitrogen and phosphorus, employing dopamine and ammonium phosphate as precursors while simultaneously forming different phases of nickel phosphide (Ni_2P or $Ni_{12}P_5$) depending on the phosphorus content. This synthesis method employs solvothermal carbonization, a low-environmental-impact process, leveraging eco-friendly reactants and

synthesis conditions. By integrating nitrogen and phosphorus into the carbon structure and forming nickel phosphide concurrently, we aimed to develop a multifunctional electrocatalyst with enhanced activity for the OER. Moreover, an increase in the phosphorus content promotes the formation of hollow nanostructures, likely due to a combination of the Kirkendall and Ostwald ripening effects. These hollow structures further improve electron transfer and reduce interfacial resistance, enhancing the catalytic activity. Operando Raman spectroscopy revealed that the Ni_2P or $Ni_{12}P_5$ phases undergo surface transformation into nickel (oxy)hydroxide species under OER conditions, yet Ni_2P-based catalysts demonstrated superior activity and long-term stability.

2. Results and Discussion

2.1. Preparation and Physico-Chemical Characterization

The synthesis strategy of nickel phosphides in N, P co-doped carbon is illustrated in Scheme 1. The XRD diffractograms of the resulting five samples (Figure 1) reveal the effect of the P/PDA ratio on the final structure of the catalyst. When no phosphorus precursor was added during the synthesis, the only phase present in the catalyst was metallic Ni (JCPDS card No. 00-004-0850), with an additional broad peak at 25.5° typical of graphitic carbon (JCPDS card No. 00-13-0148). For a low P/PDA ratio (0.15), a phase deficient in P corresponding to the tetragonal phase of $Ni_{12}P_5$ (JCPDS card No. 01-074-1381) was observed. From P/PDA 0.3 and as the ratio increased, the hexagonal structure of Ni_2P (JCPDS card No. 00-003-0953) appeared as the most stable phase, with no additional peaks from other potential phases. Consequently, the combination of nickel (II) nitrate hexahydrate along with a higher ammonium dihydrogen phosphate content promoted the formation of the pure Ni_2P phase, a highly active phase in the OER that has been widely reported in the literature [27–29].
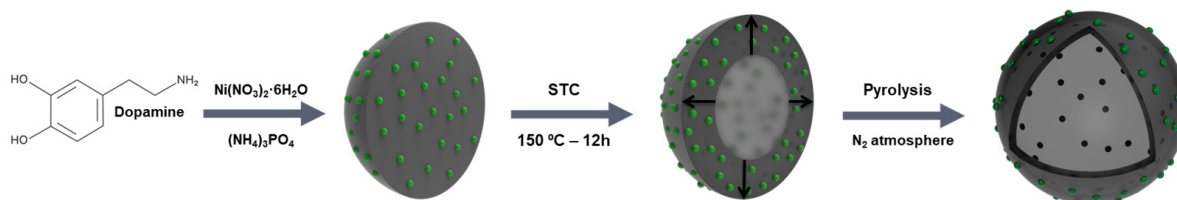
Scheme 1. Schematic illustration of the synthesis of nickel phosphides in N, P co-doped carbon.

To monitor the evolution of phase formation during the carbonization process, four catalysts with different P precursor contents (Ni, NiP 0.15, NiP 0.6, and NiP 0.9) were treated in a reaction chamber under N_2 flow from room temperature up to 900 °C. The diffractograms of the Ni sample precursor at low temperatures (below 400 °C) revealed mainly amorphous materials (Figure S1). As the temperature increased above 500 °C, the formation of the metallic Ni phase was favored, alongside the emergence of an ordered carbon structure from 700 °C. For the NiP 0.15 and NiP 0.6 catalysts, the diffraction patterns measured at different temperatures are represented in Figures 2a and 2b, respectively. At lower temperatures (≤200 °C), the primary diffraction peaks correspond to the $NiNH_4PO_4 \cdot H_2O$ phase (JCPDS card No. 00-050-0425), confirming its role as a critical precursor phase in the synthesis of NiP materials during the solvothermal process. The decomposition of $NiNH_4PO_4 \cdot H_2O$ can be observed through the loss of its characteristic peaks with the temperature. In the NiP 0.15 catalyst, new diffraction peaks appeared at 200 °C, indicating a mixture of various ammonium or nickel polyphosphate phases, along with nickel pyrophosphate. However, accurately assigning the specific diffraction peaks continues to be challenging. The in situ XRD studies at higher temperatures revealed distinct phase evolution behavior for the NiP 0.15 and NiP 0.6 catalysts. For NiP 0.15,

diffraction peaks corresponding to metallic Ni emerged at 600 and 700 °C. However, these peaks nearly disappeared upon reaching 800 °C, where the predominant phase was $Ni_{12}P_5$, which remained stable up to 900 °C. On the other hand, the transformation in the NiP 0.6 catalyst followed a different pathway. At 800 °C, a mixture of phases was observed, including $Ni_2P_2O_7$, Ni_3P, and $Ni_{12}P_5$. By 900 °C, these phases transformed mainly into Ni_2P, which became the dominant and stable phase. The NiP 0.9 catalyst suffered a similar transformation to that of NiP 0.6, with the formation of the Ni_2P at high temperatures and a stable phase after cooling down (Figure S2).
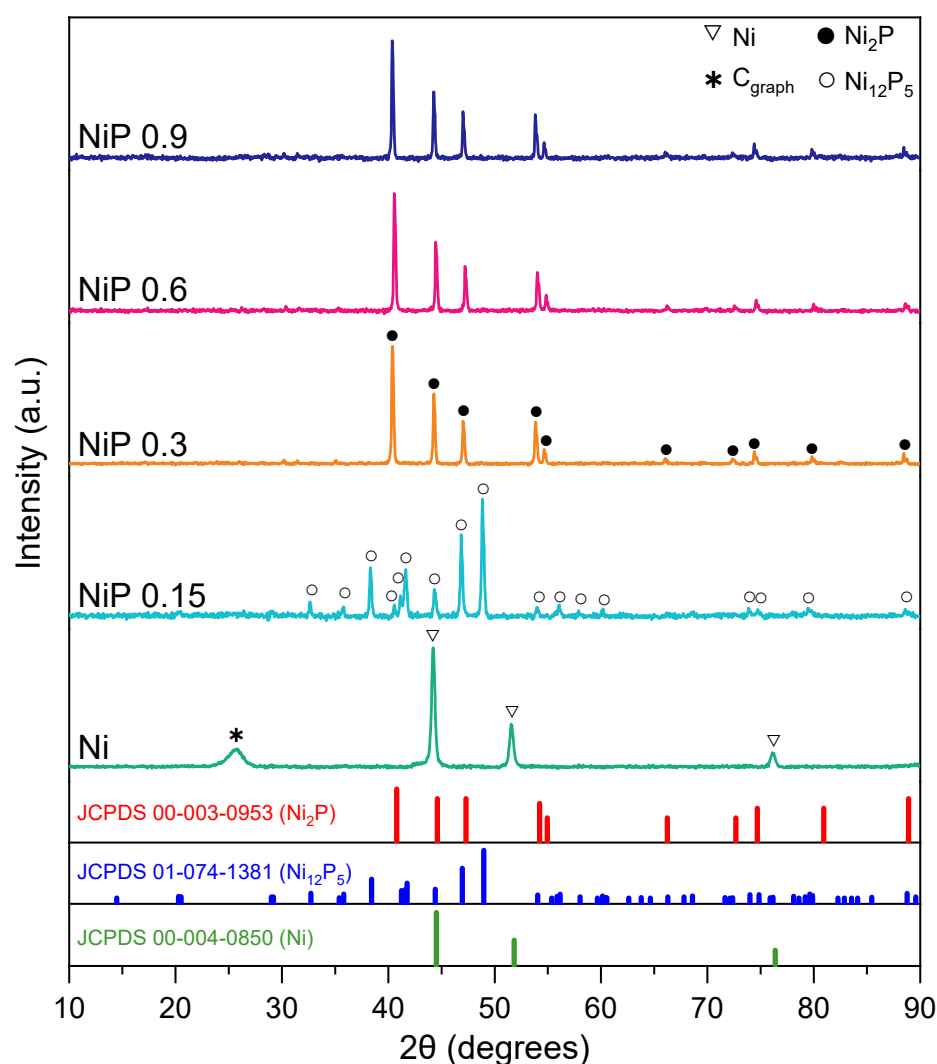

Figure 1. JCPDS cards and XRD patterns of the prepared catalysts synthesized with different P/PDA ratios.

As the result of the XRD analysis, the P/PDA ratio is critical in determining the nickel phosphide crystalline phases. For P/PDA at 0.15, the precursors have insufficient P to yield pure Ni_2P, and the resulting catalyst leads to $Ni_{12}P_5$. To prepare the Ni_2P phase, a higher amount of ammonium phosphate is required.

X-ray absorption spectroscopy (XAS) was used to further probe the bonding configuration and electronic structure of the nanocomposites. Figure 3a illustrates the characteristic Ni K-edge XANES spectra of the Ni foil together with the Ni, NiP 0.15, and NiP 0.6 synthesized catalysts. The maximum of the first-derivative peak for Ni, NiP 0.15, and NiP 0.6 appeared at 8333 eV, indicating that Ni^0 was present. Figure 3b shows the Ni K-edge EXAFS Fourier transforms (FTs) of the Ni, NiP 0.15, and NiP 0.6 synthesized samples, in

addition to the Ni foil. A remarkable difference was observed when P was introduced as a co-dopant. For the Ni sample, the FT spectra showed one strong peak at ~2.15 Å (without a phase correction) corresponding to the Ni−Ni distance characteristic of metallic nickel. The NiP 0.15 and NiP 0.6 catalysts showed a weak peak at around 1.8 Å, which increased in intensity as the P content increased. This peak can be associated with Ni-P bonding, in good agreement with the previously described structures. The apparent shift of the Ni-Ni peak to shorter distances for NiP 0.15 was probably an artifact of the broader, less defined peak shape for the sample. In order to elucidate the coordination environment of the Ni, EXAFS fits were performed and the results are shown in Figures S3–S5. The best fits that achieved the lowest R_f factor (Tables S1–S3) were obtained for the $Ni_{12}P_5$ and Ni_2P structures for NiP 0.15 and NiP 0.6, respectively, in good agreement with the results obtained in the diffraction experiments.
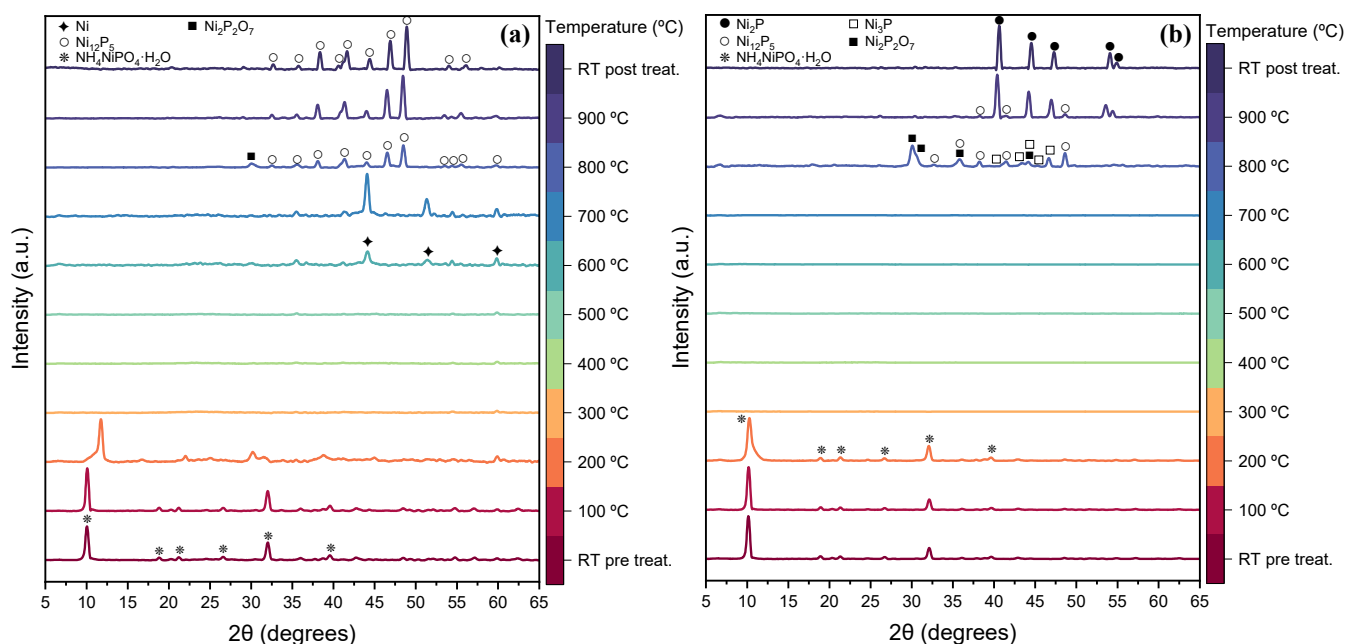

Figure 2. Evolution of the different phases formed when increasing the temperature during the pyrolytic treatment of the NiP 0.15 precursor (**a**) and the NiP 0.6 precursor (**b**) in a N_2 atmosphere.
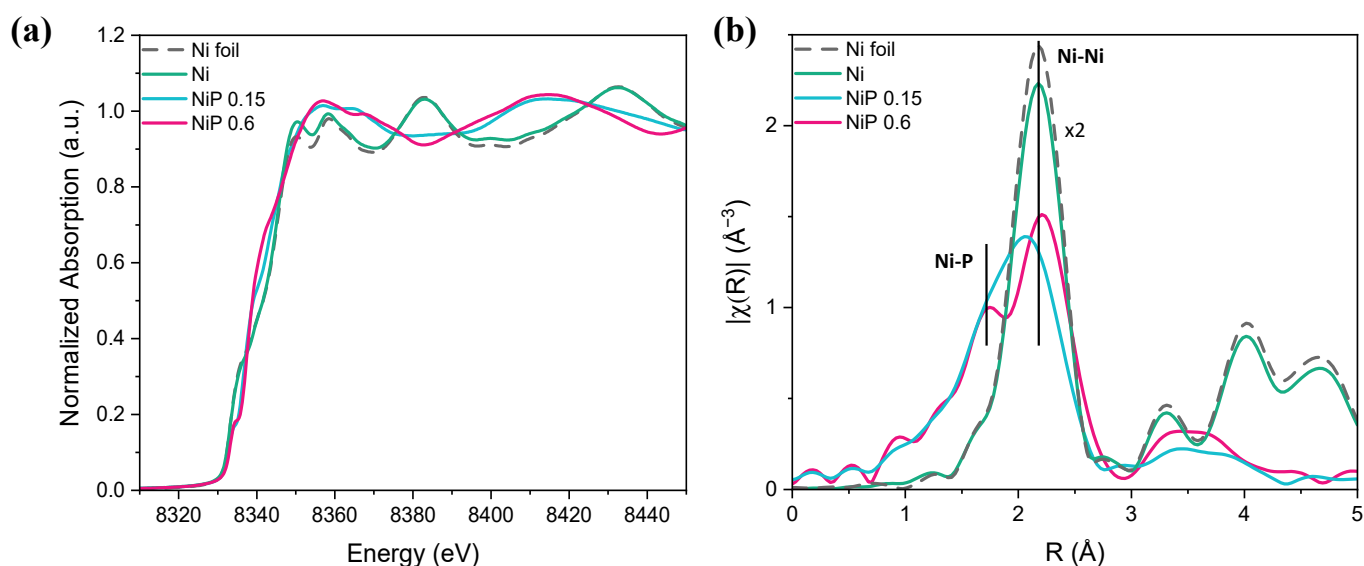

Figure 3. Normalized XANES spectra (**a**) and EXAFS Fourier transforms of $k^3\chi(k)$ functions (**b**) for Ni, NiP 0.15, and NiP 0.6 at the Ni K-edge.

Table 1 summarizes the results of the chemical composition analysis performed on the samples prepared with different P/PDA ratios and the samples without phosphorus. The presence of P favored the fixation of N, as evidenced when comparing the sample Ni with the P-containing ones. A similar effect was previously observed by Choi et al. [26], where the addition of phosphoric acid to the dicyanamide precursor composite assisted nitrogen doping into carbon. Also, phosphorus was effectively incorporated into the compound, forming the aforementioned phases, Ni_2P and $Ni_{12}P_5$.

Table 1. Chemical composition of the prepared catalysts (wt.%).

Sample	C	N	Ni	P	P/Ni
Ni	75	1.7	19	0.0	-
NiP 0.15	58	5.1	18	4.5	0.25
NiP 0.3	50	4.0	22	8.1	0.36
NiP 0.6	51	3.7	19	8.2	0.43
NiP 0.9	48	3.0	16	7.5	0.46

The transition from $NiNH_4PO_4 \cdot H_2O$ to Ni_2P by pyrolytic treatment was previously studied by Berhault et al., who described the mechanism, including the emergence of phosphate/phosphide intermediates [30]. They observed that the reduction process transitioned through three main phases: (1) The initial phase (up to 250 °C) occurs, in which the structure of $NiNH_4PO_4 \cdot H_2O$ is retained, though minor amorphization starts around 200 °C. (2) Complete amorphization occurs (300–500 °C), forming α-$Ni_2P_2O_7$. This transformation involves simultaneous dehydration and NH_3 elimination without direct reduction through the following reaction:

$$NiNH_4PO_4 \cdot H_2O \rightarrow 1/2\ Ni_2P_2O_7 + NH_3 + 3/2\ H_2O \tag{1}$$
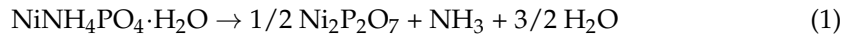
(3) Ni_2P forms selectively by 650 °C, completing the reduction. The small differences in the temperature transformation process observed for NiP 0.6 may stem from the inert environment used in our experiments, in contrast to the H_2 environment used by Berhault. In contrast, Rodriguez et al. found that the reduction mechanism included the formation of metallic nickel (Ni^0) as an intermediate step [31]. This metallic phase then reacted with residual phosphate at elevated temperatures, resulting in the formation of both Ni_2P and $Ni_{12}P_5$. The key distinction in their study was the use of a lower P/Ni ratio.

In light of our findings and previous studies, it is evident that the phosphorus content in the precursor plays a decisive role in the reduction pathway of $NiNH_4PO_4 \cdot H_2O$. In cases where the phosphorus content is sufficiently high, the reduction proceeds via the formation of α-$Ni_2P_2O_7$, as observed in our XRD analysis. This pathway involves the simultaneous elimination of ammonia and water, which agrees with the mechanism that Berhault proposed. Conversely, when the phosphorus content is lower, the reduction mechanism diverges. As reported by Rodríguez et al. [31], a phosphorus deficiency promotes the premature formation of metallic nickel, which subsequently reacts with the residual phosphate at higher temperatures to form nickel-rich phases such as $Ni_{12}P_5$. These contrasting pathways underscore the importance of maintaining an optimal P/Ni molar ratio to achieve the selective and efficient formation of Ni_2P. Furthermore, the synthesis process was significantly more sustainable in our case, as it did not require hydrogen during pyrolysis to drive the transformation. Instead, the reduction successfully occurred in an inert nitrogen atmosphere, highlighting an environmentally friendly and energy-efficient alternative for catalyst preparation. Another key difference is that our approach incorporated polydopamine, which was absent in previous studies. This addition not only introduced

nitrogen and carbon into the system, but may have also contributed to unique structural or functional properties that distinguish our materials from those reported previously.

The surface chemistry of the prepared catalysts was analyzed by X-ray photoelectron spectroscopy (XPS). Figure 4 shows the analysis of the N 1s, Ni 2p, and P 2p spectra for the range of samples with Ni, NiP 0.15, and NiP 0.6 (the spectra for the rest of the catalysts can be found in Figure S6). The survey scan of the samples revealed the presence of N and P in the catalyst's surface and the Ni from the expected metal nanoparticles employed. In the high-resolution spectrum for N 1s, four main peaks can be observed for all catalysts (Figure 4a,c,f). The pyridinic N, with a binding energy (BE) of 398.2 eV, and the N-Ni bonding at 399.4 eV were the same for all three catalysts presented [32]. Pyridinic N has been described to improve the catalytic performance due to the activation of surrounding carbon atoms [33]. Quaternary N at around 400.9 eV is presented as the main contribution in the N spectrum [34], maintaining the structure from the PDA precursor. The presence of a peak at approximately 402.6 eV corresponding to NO_x has been previously reported as the result of the pyrolytic preparation of N-doped carbons [35]. For the Ni 2p region of the Ni catalyst (Figure 4b), a predominant peak appeared at 853.2 eV, which can be associated with metallic Ni [36]. When doping with P, this peak could be assigned to the Ni metal, and a new one associated with the nickel phosphides formed due to the proximity of the BE values reported [37–39]. The deconvolution of the Ni 2p spectrum for NiP 0.6 (Figure 4g) generated four peaks. The first peak at 853.6 eV demonstrated the presence of Ni_2P, as it can be attributed to $Ni^{\delta+}$ in Ni-P bonding [40]. The BE at 855.7 eV can be assigned to Ni^{2+} in $Ni(OH)_2$ and NiO, resulting from the oxidation of the Ni_2P surface in air [41]. The peaks at 859.3 and 862.1 eV were assigned to satellite peaks [37,42]. The P 2p spectrum of NiP 0.6 (Figure 4h) showed two peaks at 129.7 and 130.6 eV, corresponding to P $2p_{3/2}$ and P $2p_{1/2}$ binding energies, respectively. The presence of these peaks matched the metal bonded with phosphorus, which indicates the proper formation of the crystalline phase Ni_2P, consistent with the XRD results above. Two other peaks at 132.2 and 133.6 eV can be assigned to the P-C and P-O groups, respectively; they manifest the successful incorporation and P-doping of the carbonaceous matrix, which could enhance the electron transfer [43,44].

The textural properties of the catalysts were characterized by nitrogen adsorption–desorption isotherms (Figure S7). The isotherm of the non-P-doped sample corresponded to the type IV isotherm, which is characteristic of mesoporous solids. The marked hysteresis loop in the Ni sample is typically associated with capillary condensation in the mesoporous structure. The other four P-doped catalysts exhibited a combination of type I and type IV isotherms. The hysteresis loops in the P/P^0 range of 0.4–0.9 for these samples indicated that the materials not only had a microporous structure, but also a mesoporous one. When comparing the areas obtained for the different P/PDA ratios (Figure 5), it was observed that incorporating a low concentration of P significantly reduced both the BET surface area and the micropore area. However, the initial micropore area was recovered and even increased when the ratio was 0.3 or higher, reaching a maximum value of 253 $m^2 \cdot g^{-1}$ for the NiP 0.9 sample. The same trend was observed for the micropore volume, which decreased significantly for low concentrations of the P precursor and increased up to a value of 0.095 $cm^3 \cdot g^{-1}$ for a 0.9 P/PDA ratio. The gradual growth of both the BET specific surface area and the micropore area with the phosphorus content has already been reported in the preparation of phosphorus-doped carbon xerogels. It has been previously observed that the increase in the specific surface area, total pore volume, and average pore size of the phosphorus-doped carbon (P-C) samples is primarily due to phosphoric acid activation, as phosphoric acid acts as an activating agent for carbon activation [45]. However, in our study, we used a more sustainable chemical compound, ammonium phosphate, to achieve this carbon activation.
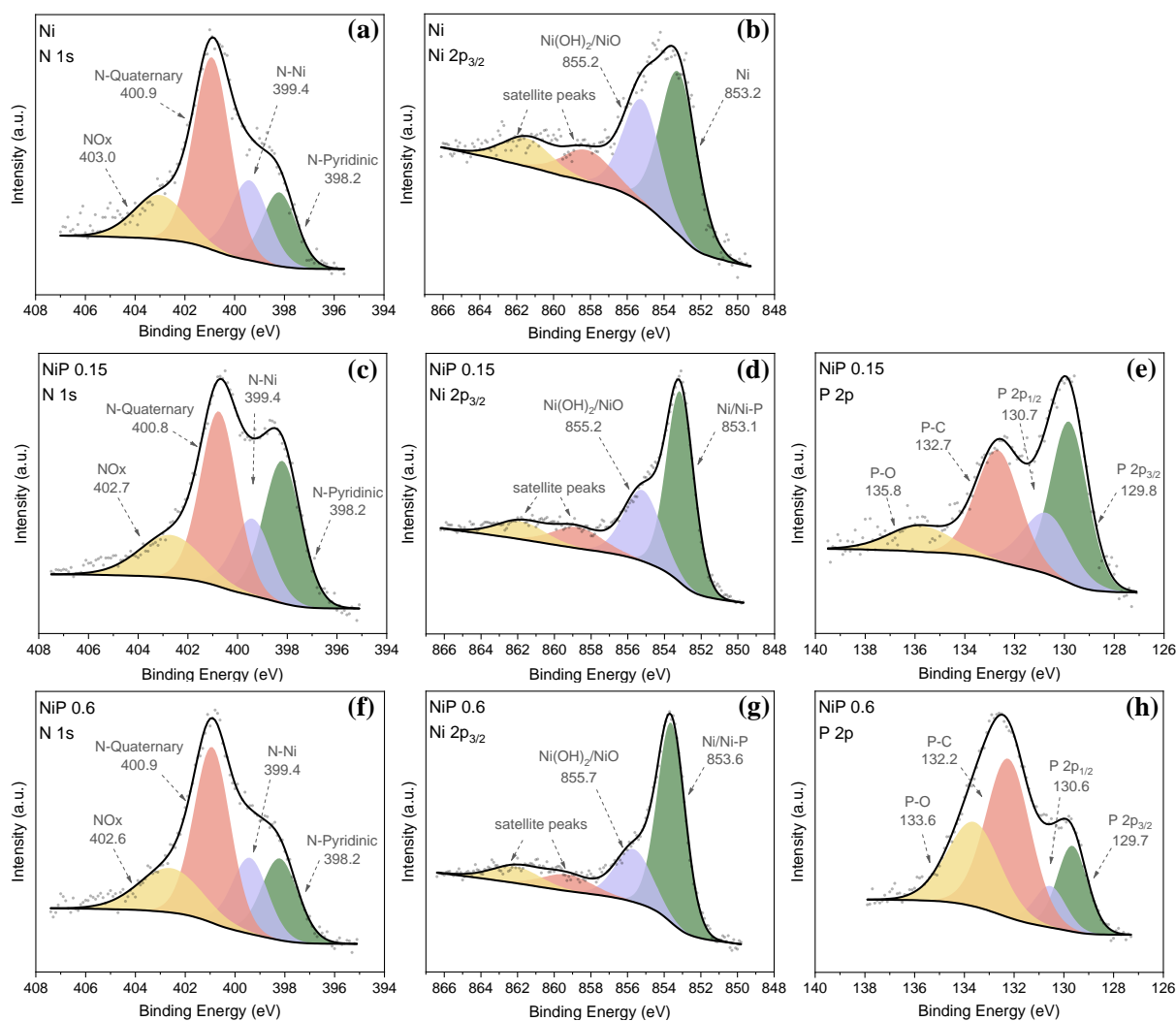
Figure 4. XPS spectra range and deconvolution corresponding to N 1s (**a**) and Ni 2p (**b**) for Ni; N 1s (**c**), Ni 2p (**d**) and P 2p (**e**) for NiP 0.15; and N 1s (**f**), Ni 2p (**g**), and P 2p (**h**) for NiP 0.6.
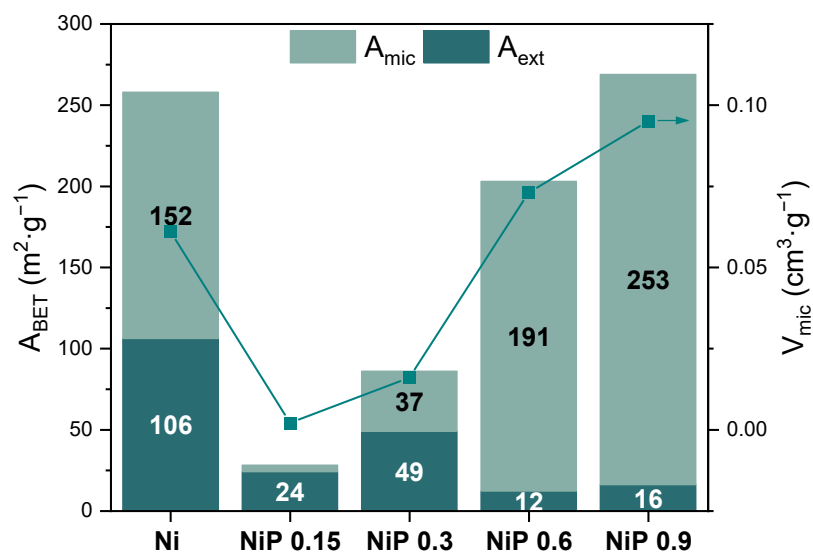

Figure 5. Variation in micropore volume and external and micropore area for all catalysts.

For TEM investigations, the electrocatalysts were dripped directly onto a lacey carbon-coated copper grid, and the plasma was cleaned just before being inserted into the microscope. We performed a STEM analysis at a 200 kV accelerated voltage with an extended

monochromator to minimize the effect on sample damage. TEM images of all the electrocatalysts are shown in Figure 6. For the sample prepared without phosphorus (Figure 6a), the formation of a nanocomposite by Ni nanoparticles with a wide size distribution within a compact carbonaceous matrix can be observed. When phosphorus was incorporated in low concentrations, from P/PDA ratios of 0.15 to 0.3 (Figures 6b and 6c, respectively), the carbon matrix seemed to be denser with no presence of any porous structure, consistent with the decrease in the area observed in N_2 adsorption–desorption experiments. However, a hollow structure emerged as the quantity of the dopant increased. As seen in the NiP 0.6 and NiP 0.9 samples, shown in Figures 6d and 6e, respectively, this led to perfectly shaped hollow spheres with smaller Ni-containing nanoparticles embedded into their walls. The formation of this morphology resulted in an increase in the specific surface area, particularly the micropore area, as calculated from the adsorption–desorption isotherms. This type of microporosity has been previously reported for hollow carbon sphere synthesis [46,47].
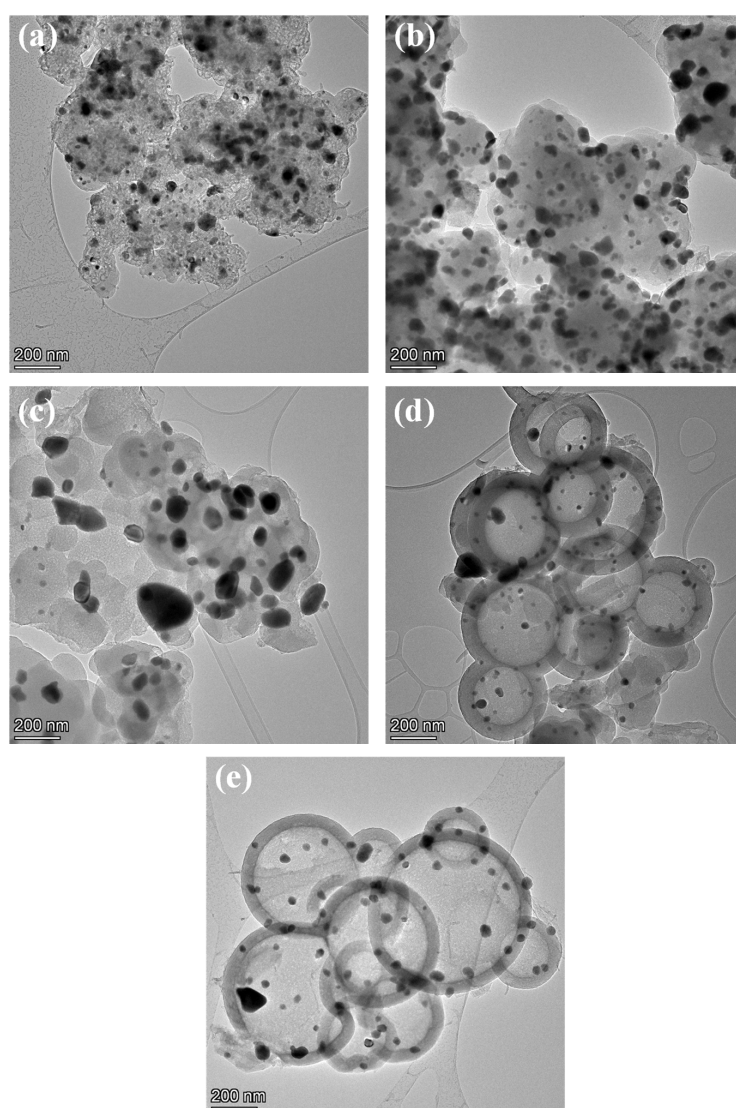

Figure 6. TEM images for Ni (**a**), NiP 0.15 (**b**), NiP 0.3 (**c**), NiP 0.6 (**d**), and NiP 0.9 (**e**).

Additional electronic microscopy studies were carried out for the Ni and NiP 0.6 samples to further investigate the formation of these nanostructures. In the first instance, these catalysts were analyzed by TEM before and after the pyrolytic process (Figure S8a–d). The Ni catalyst exhibited an amorphous structure prior to pyrolysis, which transitioned to a slightly deformed, small-sized spherical carbon structure after pyrolysis. In contrast,

for the NiP 0.6 catalyst, these spherical structures were already observed after the hydrothermal treatment and remained present following the pyrolysis process, which was confirmed using STEM images collected with BF and HAADF detectors (Figure 7). The hollowness of these structures was evident when a linear analysis of the composition along the microstructure was performed (Figure S9). It was confirmed that the formation of the hollow sphere architecture in NiP 0.6 before pyrolysis was promoted by adding P during the solvothermal reaction. The formation of these distinctive structures can be attributed to the Kirkendall effect [48–51]. During this process, the imbalance between the diffusion of atoms and ions from the core and the reaction at the interface allowed for the formation of vacancies within the structure. During solvothermal process heating, these vacancies coalesced, resulting in hollow sphere morphologies. It is worth mentioning the absence of defined Ni or Ni_2P nanoparticles for the NiP 0.6 non-pyrolyzed sample. For reliable quantitative results, EDS mapping with a diminished monochromator was used. According to the EDS map of the NiP 0.6 sample before pyrolysis, it was noticeable that N, Ni, and P (Figure 7c, Figure 7e, and Figure 7f, respectively) were homogeneously dispersed throughout the spherical structure, without larger aggregates.
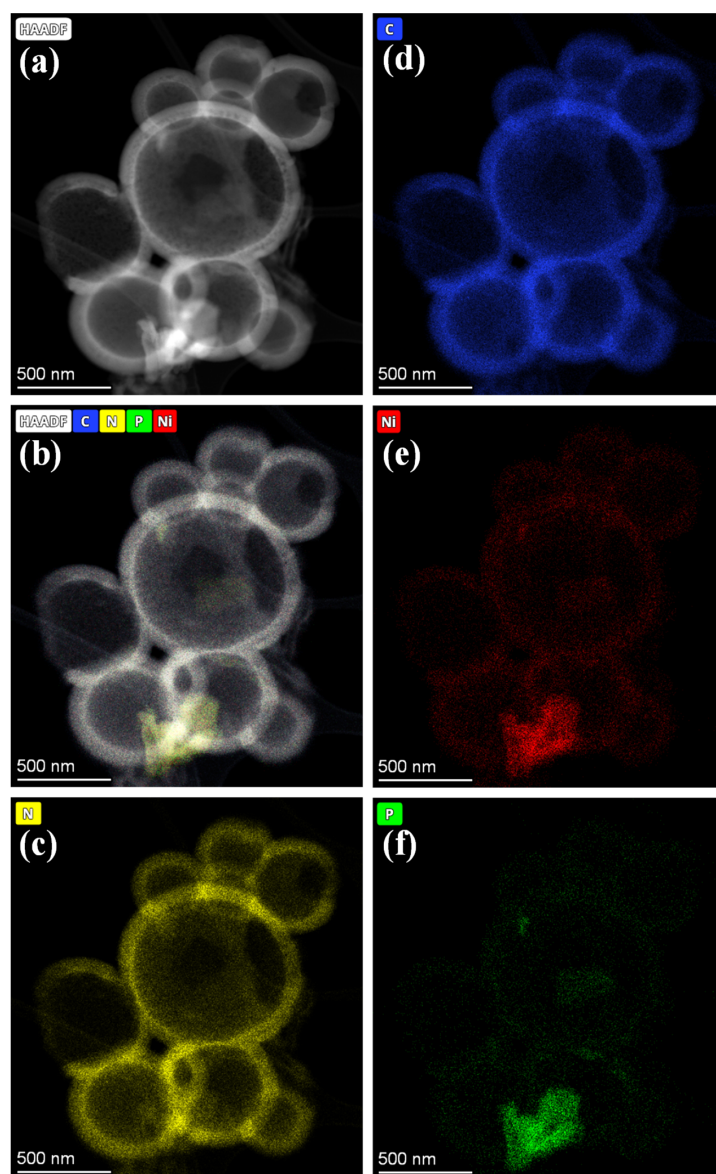

Figure 7. HAADF-STEM image (**a**) for NiP 0.6 catalyst before pyrolysis. EDS combined map (**b**) and individuals for N (**c**), C (**d**), Ni (**e**), and P (**f**).

As a result of the heating during the pyrolysis stage, the Ni dispersed through the structure suffered a process known as Ostwald ripening [51], which implies the redissolution of metal structures and diffusion to form larger particles, such as those evidenced on the final catalysts. This phenomenon occurs due to the fact that larger particles are energetically favored over smaller particles [50]. The particles crystallized in the metallic Ni and Ni_2P phases for the Ni and NiP 0.6 samples, respectively, according to the SAED experiments (Figure S10). Regarding the carbon structure, the Ni sample images provided evidence of an order of layers surrounding the Ni particles, an arrangement that disappeared with the P doping, leading to amorphous C. This difference was also reflected in the XRD patterns, with the emergence of the ordered C peak only for the non-doped catalyst.

Figure 8 shows the EDS map for the pyrolyzed NiP 0.6. Upon analyzing the images and the linear analysis (Figure S11), the formation of hollow C spheres was confirmed. It is possible to appreciate in Figure 8f that phosphorus atoms are not only present as a part of the Ni_2P particles, as the red and green colors overlap in the largest Ni particles, but they also fit with the blue shading of C in Figure 8d. Similarly, the elemental map of N (Figure 8c) fits perfectly with that of C, revealing the prevalence and high dispersion of the heteroatom in the carbonaceous phase. This suggests the doping of the carbonaceous structure, one of the main goals of the proposed synthetic strategy. Therefore, the proposed synthetic strategy successfully achieved both the formation of nickel phosphide and the simultaneous doping of carbon with phosphorus.
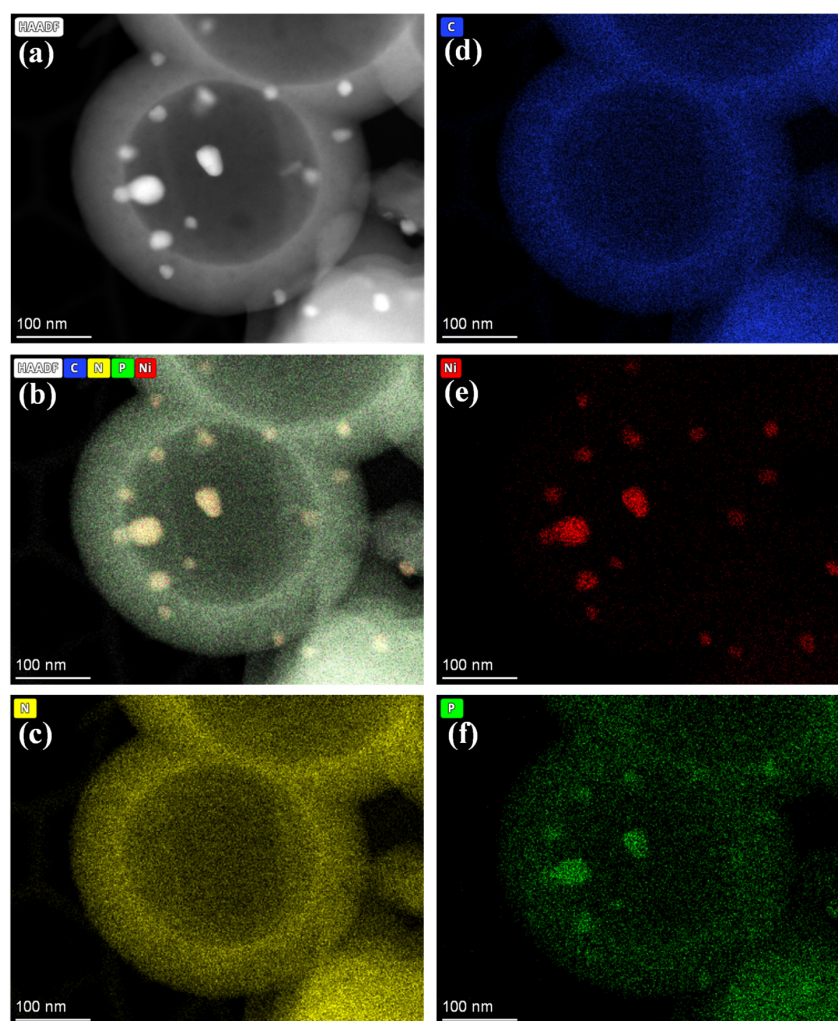

Figure 8. HAADF-STEM image (**a**) for NiP 0.6 catalyst after pyrolysis. EDS combined map (**b**) and individuals for N (**c**), C (**d**), Ni (**e**), and P (**f**).

2.2. Electrochemical Characterization: OER Studies

Figure 9a shows the polarization curves obtained during the OER evaluation experiments for the samples prepared with different P/PDA ratios. The data extracted from the graphs are summarized in Figure 9b. The prepared catalysts presented values similar to IrO_2, which is usually used as a benchmark, with a remarkable overpotential of 405 mV for the NiP 0.6 sample, only 4 mV above the iridium oxide catalyst in the 0.1 M NaOH electrolyte [52]. Notably, there was a broad peak observed at over 1.4 V vs. RHE, which displayed a higher intensity in catalysts with P/PDA ratios of 0.3 or greater. This oxidation peak shows the redox transition of $Ni(OH)_2$/NiOOH (Ni^{II}/Ni^{III}), which appeared in the potential region of 1.3–1.5 V vs. RHE and was identified as the actual active site for OER [53]. Since these catalysts exhibited the Ni_2P crystalline phase, the transition from Ni_2P to an oxygen-rich surface was likely responsible for the enhanced catalytic performance of the prepared electrocatalysts in this study [29,54]. This interface enables efficient charge carrier transfer, where the phosphide core acts as an excellent electrical conductor. At the same time, the (oxy)hydroxide overlayer formed during catalytic transformation enhances electron transport [13]. Therefore, the designed synthetic methodology possesses the potential for the construction of fit-for-purpose catalysts through a green chemistry strategy. The Tafel plots, shown in Figure S12, revealed a reduction in the slope from 134.5 mV dec^{-1} for the Ni catalyst to 81 mV dec^{-1} upon the incorporation of phosphorus in the NiP 0.15 catalyst, thereby enhancing the reaction kinetics. However, the slope increased to approximately 120 mV dec^{-1} for the NiP 0.6 and NiP 0.9 catalysts. The high microporosity may have limited the kinetics due to the impediment of the diffusion of reactive species (OH^- and O_2) inside the micropores [55].
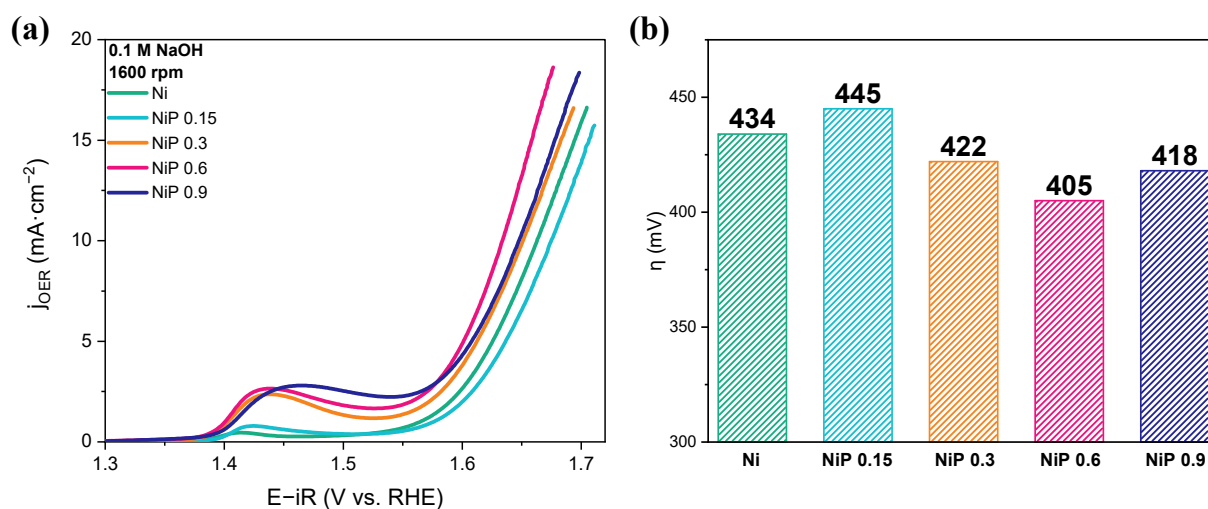

Figure 9. OER polarization curves of samples prepared with different P/PDA ratios in an Ar-saturated 0.1 M NaOH electrolyte at 1600 rpm with an iR correction (**a**) and overpotentials, η, calculated for the prepared samples at 10 mA·cm^{-2} (**b**).

An analysis of the electrochemical impedance spectroscopy (EIS) data was carried out to understand the role of phosphorus in the efficiency of the OER reaction. The Nyquist plots obtained can be observed in Figures 10 and S13. For all the studied catalysts, two depressed semicircles were observed. The main differences were evidenced by the semicircle at lower frequencies, a region usually related to the charge transfer processes. A small quantity of P led to the growth of the semicircle, which was associated with a higher resistance. As the content of P increased, this resistance was lowered, with the minimum observed for the NiP 0.6 sample. To extract more precise information from the EIS measurements, the data were fitted by using the equivalent electrical circuit (EEC) shown

in the inset, employed previously by Lyons and Brandon for OER electrocatalysts [56]. In this diagram, R_s refers to the solution resistance. Q_1/R_1 and Q_2/R_2 are related to the kinetics of surface processes, including electroadsorption and electrodesorption. Finally, C_{dl} considers the double-layer capacitance on the surface during the electrochemical reaction and R_{ct} is the resistance associated with the charge transfer. Table S4 summarizes the calculated values of R_{ct} for the tested electrocatalysts at different potentials. As predicted through the Nyquist plots, NiP 0.6 presented the lowest resistance for the charge transfer independently of the selected potential. In addition to the well-established performance of Ni phosphides as OER electrocatalysts [57,58], doping the carbon matrix with both N and P has been reported to enhance electrical conductivity and reduce the charge transfer resistance. This improvement was attributed to changes in the local charge density and spin density asymmetry, enhanced by the available electron pair in phosphorus [59,60]. Furthermore, the hollow structures of the doped carbon can provide superior electron transfer and lower interfacial resistance, contributing to overall enhanced catalytic activity.
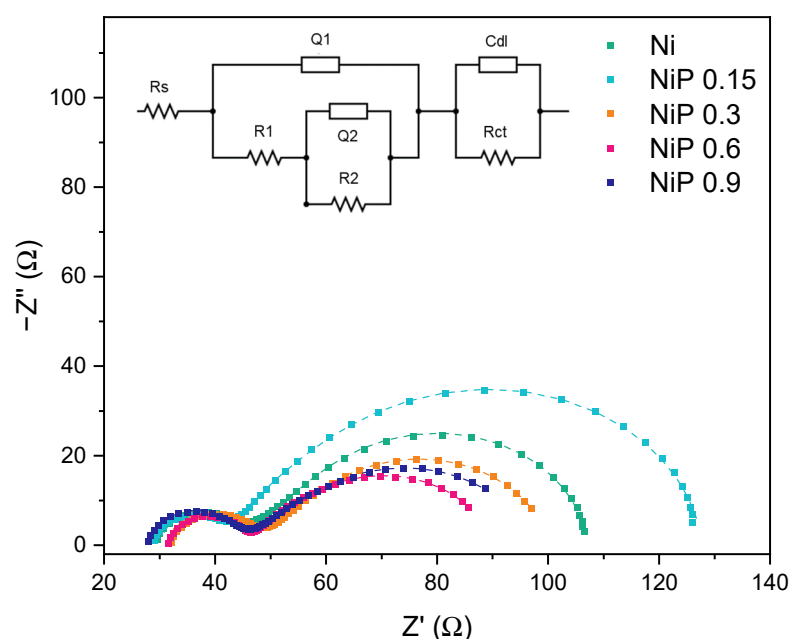

Figure 10. Nyquist plots for the catalysts prepared with different P/PDA ratios at −1.6 V vs. RHE. Inset: EEC employed for data fitting.

The electrochemical surface area (ECSA) was evaluated to explain the differences between the catalysts' performance. It was estimated from the Nyquist plots of the EIS experiments by using the following equations:

$$C_{dl} = \frac{1}{2\pi f R_{ct}} \tag{2}$$

$$\text{ECSA} = \frac{C_{dl}}{C_s} \tag{3}$$

where C_{dl} is the double-layer capacitance (in F), f (in Hz) is the frequency value at the maximum of the charge transfer semicircle of the imaginary part of impedance ($-Z''$), and C_s is the specific capacitance, typically 0.04 mF·cm^{-2}, as observed in previous literature [61–63]. The ECSA increased significantly across the studied catalysts, with NiP 0.6 exhibiting the highest ECSA (363 cm^2), followed by NiP 0.9 (245 cm^2) and NiP 0.3 (142 cm^2), while Ni and NiP 0.15 displayed much lower values (44 cm^2 and 43 cm^2, respectively). The increase in the available area may be linked to the formation of hollow spheres. These results

align perfectly with the improvement in the OER overpotential for the NiP 0.6 and NiP 0.9 catalysts, enhancing rapid electrolyte diffusion. The calculated values are comparable to those previously reported in the literature for electrocatalysts based on nickel phases on carbon [63,64].

An operando Raman investigation was performed on the Ni, NiP 0.15, and NiP 0.6 catalysts to identify the composition of the actual catalytic species under OER conditions (Figure 11). In the Raman spectra, all the catalysts exhibited two characteristic bands close to 470 and 550 cm^{-1}, corresponding to the Ni-O vibrations in NiOOH [29,53]. These bands were only observed at the potentials of 1.35 V and 1.40 V in the Ni catalyst. In contrast, for the NiP 0.15 catalyst, these bands began to appear at a lower potential of 1.20 V with a low intensity, which increased between 1.4 and 1.5 V, decreasing again up to 1.6 V. Meanwhile, in the case of the NiP 0.6 catalyst, these bands emerged at 1.40 V and became increasingly intense as the potential increased up to 1.60 V. Therefore, the catalytically active site in NiP 0.6 are likely associated with the formation of nickel (oxy)hydroxide species. These results indicate that Ni$_2$P could act as a highly efficient precatalyst for the OER. This is consistent with the behavior observed for other Ni$_2$P OER electrocatalysts [29,65]. The NiP/NiOOH heterojunction facilitates electron transfer and accelerates OER kinetics, further contributing to the superior performance of the NiP 0.6 catalyst.
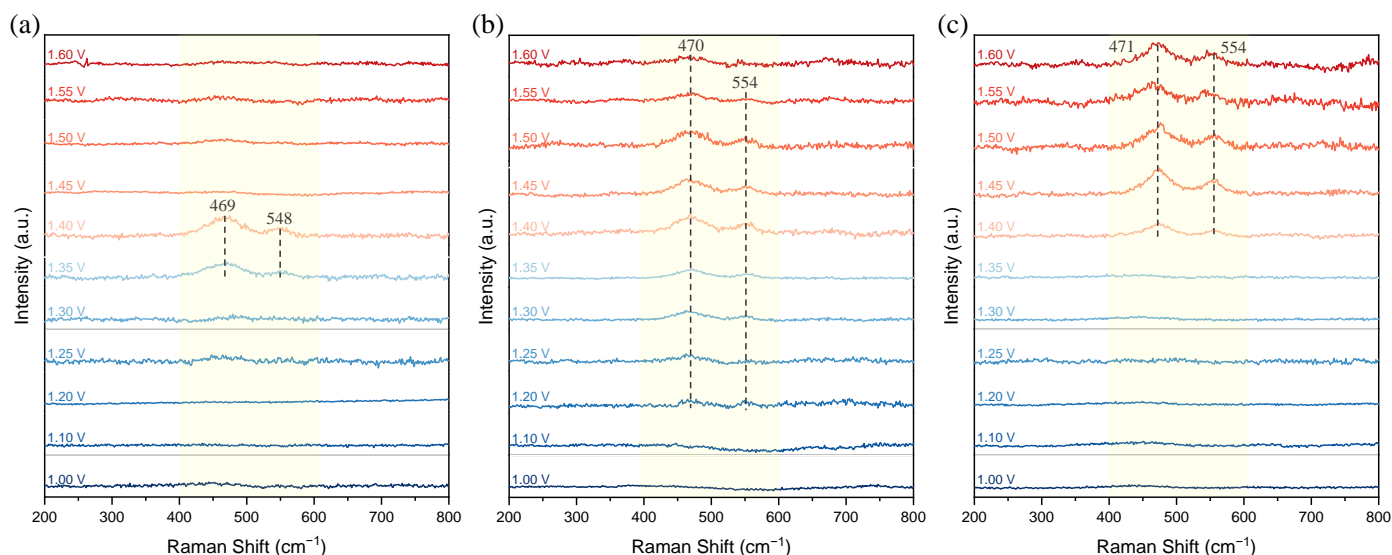

Figure 11. Operando Raman spectra of the Ni (**a**), NiP 0.15 (**b**), and NiP 0.6 (**c**) catalysts collected in the potential range of 1.0–1.60 V vs. RHE.

To assess the electrocatalytic stability of the NiP 0.6 catalyst, we conducted chronopotentiometry measurements in O$_2$-saturated 0.1 M NaOH at a current density of 10 mA·cm^{-2}. The results only show a slight decrease in the potential after more than 24 h of the oxygen evolution reaction test, as illustrated in the E–t response curve in Figure 12. These findings confirm that the NiP 0.6 catalyst is highly durable and exhibits high activity even after long-term testing.

In summary, the addition of P to the catalysts, both forming nickel phosphides and bonding to C as observed through XAS and XPS experiments, respectively, has proven to be a valid strategy for improving the performance of these materials as OER electrocatalysts. NiP 0.6 and NiP 0.9 both feature a hollow carbon morphology and a dominant Ni$_2$P phase, which enhances NiOOH stability. However, NiP 0.9 showed a slightly higher resistance, possibly due to mass transport limitations in excessive microporosity. On the other side, NiP 0.15, despite forming NiOOH over a broad voltage range (1.20–1.60 V), exhibited poor OER activity due to its Ni$_{12}$P$_5$ phase, which seemed to be less active for OER. A comparison

of different catalysts reported in the literature based on their overpotentials is included in Table S5.
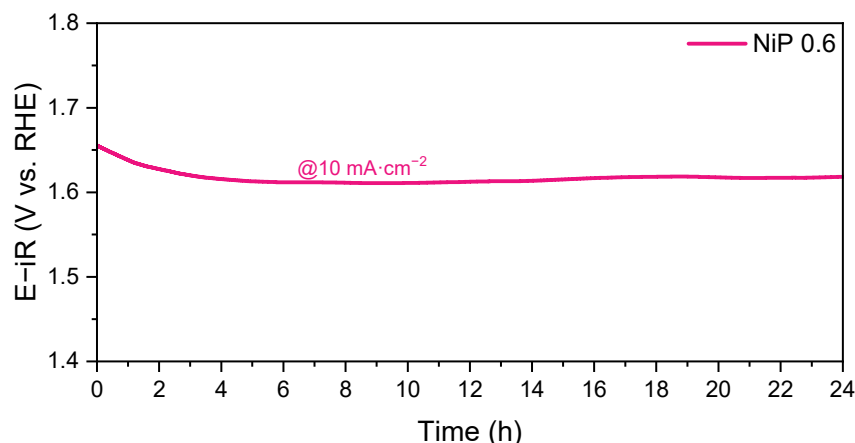

Figure 12. Chronopotentiometry measurement of NiP 0.6 catalyst.

3. Materials and Methods

3.1. Materials

The following products were employed without any further purification: nickel (II) nitrate hexahydrate (Alfa aesar, Kandel, Germany, 98%), dopamine hydrochloride (Sigma-Aldrich, Steinheim, Germany), ammonium dihydrogen phosphate (Acros organics, Geel, Belgium, 98+%), and ammonia solution (Merck, Darmstadt, Germany, 28–30%). Sodium hydroxide (Sigma-Aldrich, St. Louis, MI, USA 99.99%), absolute ethanol (Scharlab, Barcelona, Spain, 99.9%), and Nafion® perfluorinated resin (Sigma-Aldrich, Steinheim, Germany, 5 wt.%) were used during the electrochemical characterization.

3.2. Synthesis of Nickel Phosphides in N, P Co-Doped Carbon

The catalysts were prepared using a modified solvothermal carbonization method with polydopamine developed by our research group [66]. For this purpose, 0.257 g of nickel (II) nitrate hexahydrate and 0.57 g of dopamine hydrochloride were dissolved in 95 mL of absolute ethanol and 8 mL of distilled water for 24 h under continuous magnetic stirring. The quantity of ammonium phosphate varied to prepare samples with different P/PDA weight ratios (0, 0.15, 0.3, 0.6, and 0.9), and it was also dissolved in distilled water together with the rest of the reagents. The resulting solution was transferred into a 150 mL Teflon-lined stainless-steel autoclave and maintained at 150 °C for 12h in a solvothermal process. Once finished, the reactor was cooled down to room temperature, and the suspension was centrifuged and washed 4 times with absolute ethanol and water. The obtained suspension was left to dry at room temperature overnight before the heat treatment. Finally, the powder was pyrolyzed at 900 °C for two hours under a N_2 atmosphere. A heating rate of 5 °C/min was employed. The obtained black powders were labeled as Ni, NiP 0.15, NiP 0.3, NiP 0.6, and NiP 0.9.

3.3. Physico-Chemical Characterization

The nickel- and phosphorus-loading of catalysts was achieved by inductively coupled plasma atomic emission spectroscopy (ICP-OES) with a PERKIN ELMER OPTIMA 2100 DV (Shelton, USA), whereas elemental analyses (CHNS) were performed by an elemental chemical analyzer (LECO CHNS-932, Mönchengladbach, Germany).

For the structural characterization of samples, X-ray diffraction (XRD) was carried out by means of an X-Pert Pro PANalytical instrument (Worcestershire, UK) with Cu Kα radiation (1.5418 Å). The equipment was coupled to a reaction chamber (Anton Paar

XRK900, Graz, Austria) that allowed for the study of the phases at different temperatures and under a controlled atmosphere. The temperature ranged from room temperature to 900 °C in 100 °C steps under a N_2 flow.

The distribution and valence state of elements in the near-surface layer were determined by X-ray photoelectron spectroscopy (XPS), with the electron spectroscopy system SPECS GmbH with UHV system (pressure approx. 10-10 mbar); the energy analyzer PHOIBOS 150 9MCD; monochromatic (with double anode Al/Ag) and non-monochromatic (with double anode Al/Mg) X-ray sources; an electron source for charge compensation; a UV photon source; an ion source; and a sample pretreatment chamber. The collected spectra were calibrated with the binding energy of the C-C bond of C 1s at 284.6 eV.

The textural characterization was determined by nitrogen adsorption–desorption isotherms, which were measured on a Micromeritics ASAP 2020. The Brunauer–Emmet–Teller (BET) method was applied to calculate specific surface areas, and the Barret–Joyner–Halenda (BJH) method was used to obtain the pore size distributions.

Transmission electron microscopy (TEM) images were obtained using a C_s S-CORR probe corrected Spectra 300 (ThermoFisherScientific, Waltham, MA, USA) scanning transmission electron microscope (S/TEM) at a 200 kV accelerating voltage. The microscope was equipped with a C_s S-CORR probe corrector, a 4×30 mm^2 windowless Super-X EDS detector, an electron microscope pixel array detector (EMPAD), and a monochromator, which, combined with the X-FEG gun and an ultra-high stability, allowed electron energy loss spectra (EELS) to be recorded with a high energy resolution. The equipment allowed selected area electron diffraction (SAED) tests to be conducted. STEM images were recorded with high-angle annular dark-field (HAADF) and bright-field (BF) detectors. During STEM mode, a camera length of 115 mm, a beam current of 30 pA, and a 100 μm C2 aperture were used, and for EDS mapping, a beam current of 120 pA and a 70 μm C2 aperture were used. The acquisition and the post-processing data analysis were managed with the Velox software 3.15.

X-ray absorption spectroscopy (XAS) measurements were performed at room temperature at the B18 beamline of Diamond Light Source [67]. The monochromator comprised Si(111) crystals operating in Quick EXAFS mode. The calibration of the monochromator was carried out using Ni foil, and the XAFS spectra were recorded in transmission and fluorescence modes at the Ni K-edge (8333 eV) using a Canberra 36-element monolithic planar Ge pixel array detector. The spectra were aligned using the Ni foil response. The data were analyzed using the Athena and Artemis programs of the DEMETER software package version 0.9.26 [68].

3.4. Electrochemical Characterization

To evaluate the electrochemical properties of the prepared catalysts, an ink was prepared at a 10 mg·mL^{-1} catalyst concentration in absolute ethanol and 15 wt.% of Nafion$^{®}$ solution. The mixture was sonicated for 15 min to ensure homogenization. An amount of 20 μL of the prepared ink was deposited to obtain the working electrode (WE) on a rotating ring disk electrode (RRDE) with a glassy carbon disk of a 5 mm diameter (area = 0.196 cm^2) and a Pt ring of a 7 mm external diameter (collection efficiency of 24.9%). The electrochemical performance was evaluated using a 0.1 M NaOH electrolyte in a three-electrode cell configuration controlled by a potentiostat/galvanostat AutoLab workstation (PGSTAT302N). A glassy carbon rod was employed as a counter electrode (CE), and a reversible hydrogen electrode, RHE, was used in the supporting electrolyte as a reference electrode (RE). Before the measurements, the electrolyte was purged with Ar (99.995%, Air Liquide) for about 30 min to remove the presence of oxygen. During the experiments, the solution was constantly bubbled with Ar. The electrochemical activation of the catalyst was

carried out before the oxygen evolution tests. This process entailed 50 cyclic voltammetries (CVs) between 0.05 and 1.2 V vs. RHE at a scan rate of 0.1 V·s^{-1}. The activity as OER catalyst was evaluated by recording 10 CV cycles between 1.2 and 1.8 V vs. RHE (positive scan) at 0.005 V·s^{-1} and 1600 rpm. EIS was performed at -1.5, -1.55, -1.6, -1.65, and -1.70 V vs. RHE to evaluate the differences in the charge transfer process at different points of the polarization curve. A sinusoidal perturbation with a 10 mV amplitude was applied in the frequency range from 0.1 Hz to 100 kHz. The measured value of the solution resistance (R_s) was employed to correct the ohmic drop ($i \cdot R_s$).

3.5. In Situ/Operando Raman Spectroscopy

Raman spectra were recorded with a Renishaw inVia Qontor instrument equipped with a cooled CCD detector, a confocal microscope, and a 514 nm Ar ion laser. Measurements were performed using a Raman electrochemical flow cell (Redox.me) in 1 M KOH. For the preparation of the working electrode (WE), an ink was prepared at 10 mg·mL^{-1} of catalyst concentration in absolute ethanol and 15 wt.% of Nafion$^{®}$ solution. The mixture was sonicated for 15 min to ensure homogenization. A total of 6.4 µL of the prepared ink was deposited on the 2 mm glassy carbon disk of the WE and dried prior to its use. Platinum wire was used as the counter electrode, and Ag/AgCl was used as a reference electrode and reported versus the reversible hydrogen electrode (RHE) using the following Nernst equation: $E_{RHE} = E_{Ag/AgCl} + 0.210$ V $+ 0.059$ pH. An Autolab PGSTAT204 potentiostat/galvanostat was used for electrochemical measurements. Each spectrum was recorded for 90 s after the beginning of each potential step from OCP until 1.60 V vs. RHE.

4. Conclusions

We successfully synthesized nickel phosphide and N, P co-doped carbon catalysts using a sustainable solvothermal method followed by pyrolysis. The use of dopamine and ammonium phosphate as precursors effectively achieved the desired co-doping and phase formation, enabling the development of hollow structures, particularly with a higher phosphorus content. These hollow structures, formed via the Kirkendall effect and Ostwald ripening during the strategy synthesis, enhanced the specific surface area and micropore volume, facilitating better electron transfer and lower interfacial resistance. The electrochemical analysis demonstrated that the synthesized catalysts exhibited a high OER performance, with lower overpotentials than their non-doped counterparts. The enhanced catalytic activity was attributed to the presence of a Ni$_2$P/NiOOH interface. This interface enables efficient charge carrier transfer, where the phosphide core acts as an excellent electrical conductor, while the (oxy)hydroxide overlayer formed during catalytic transformation enhances electron transport. Thus, the catalyst with the best electrochemical performance, NiP 0.6, was the one able to maintain the (oxy)hydroxide signal under the entire working potential range, as evidenced by the operando Raman. Overall, this work presents a promising strategy for the development of efficient and sustainable electrocatalysts for oxide evolution reactions, significantly contributing to the advancement of energy storage technologies.

the Ni sample at the Ni K-edge. N is the coordination number, R is the interatomic distance, and σ2 is the Debye–Waller factor. Rf is the R-factor, which represents the relative error of the fit and data. 3.0 < k < 12.9; 1.0 < R < 3.0. S02 = 0.78; Figure S4: k2-weighted Fourier transform EXAFS data (a) and k2-weighted χ data (b) for the NiP 0.15 catalyst recorded at the Ni K-edge; Table S2: Relative energy shift and the best fit result (with a Ni12P5 structure, ICSD 137574) from the structural analysis of the NiP 0.15 sample at the Ni K-edge. 3.0 < k < 12.0; 1.0 < R < 3.0. S02 = 0.78; Figure S5: k2-weighted Fourier transform EXAFS data (a) and k2-weighted χ data (b) for the NiP 0.6 catalyst recorded at the Ni K-edge; Table S3: Relative energy shift and the best fit result (with a Ni2P structure, ICSD 27162) from the structural analysis of the NiP 0.6 sample at the Ni K-edge. 3.0 < k < 12.0; 1.0 < R < 3.0. S02 = 0.78; Figure S6: XPS spectral range and deconvolution corresponding to N 1s (a), Ni 2p (b), and P 2p (c) for NiP 0.3, and N 1s (d), Ni 2p (e), and P 2p (f) for NiP 0.9; Figure S7: N2 adsorption–desorption isotherms for the Ni, NiP 0.15, NiP 0.3, NiP 0.6, and NiP 0.9 catalysts; Figure S8: TEM images for Ni before (a) and after (b) pyrolysis, and for NiP 0.6 before (c) and after (d) pyrolysis; Figure S9: HAADF-STEM image (a) and EDS line-scan profiles (b) of the NiP 0.6 catalyst before pyrolysis. An EDS line scan was executed following the green line in (a); Figure S10: SAED diffractograms for the Ni (a) and NiP 0.6 (b) catalysts; Figure S11: HAADF-STEM image (a) and EDS line-scan profiles (b) of the NiP 0.6 catalyst after pyrolysis. The EDS line scan was executed following the green line in (a); Figure S12: Tafel plots derived from polarization curves; Figure S13: Nyquist plots for the catalysts prepared with different P/PDA ratios at −1.5 V (a), −1.55 (b), −1.65 (c), and −1.7 (d) V vs. RHE; Table S4: Calculated values of Rct (Ω) extracted from the fitting of the EIS data for the tested electro-catalysts at different potentials; Table S5: Comparison of oxygen evolution reaction performance of Ni-based catalysts in different electrolytes.

References

1. Vass, Á.; Kormányos, A.; Kószó, Z.; Endrődi, B.; Janáky, C. Anode Catalysts in CO2 Electrolysis: Challenges and Untapped Opportunities. *ACS Catal.* **2022**, *12*, 1037–1051. [CrossRef] [PubMed]
2. Xie, X.; Du, L.; Yan, L.; Park, S.; Qiu, Y.; Sokolowski, J.; Wang, W.; Shao, Y. Oxygen Evolution Reaction in Alkaline Environment: Material Challenges and Solutions. *Adv. Funct. Mater.* **2022**, *32*, 2110036. [CrossRef]
3. Chatenet, M.; Pollet, B.G.; Dekel, D.R.; Dionigi, F.; Deseure, J.; Millet, P.; Braatz, R.D.; Bazant, M.Z.; Eikerling, M.; Staffell, I.; et al. Water electrolysis: From textbook knowledge to the latest scientific strategies and industrial developments. *Chem. Soc. Rev.* **2022**, *51*, 4583–4762. [CrossRef] [PubMed]
4. Liu, Y.; Zhou, D.; Deng, T.; He, G.; Chen, A.; Sun, X.; Yang, Y.; Miao, P. Research Progress of Oxygen Evolution Reaction Catalysts for Electrochemical Water Splitting. *ChemSusChem* **2021**, *14*, 5359–5383. [CrossRef]

5. Dionigi, F.; Strasser, P. NiFe-Based (Oxy)hydroxide Catalysts for Oxygen Evolution Reaction in Non-Acidic Electrolytes. *Adv. Energy Mater.* **2016**, *6*, 1600621. [CrossRef]

6. Gebreslase, G.A.; Martínez-Huerta, M.V.; Lázaro, M.J. Recent progress on bimetallic NiCo and CoFe based electrocatalysts for alkaline oxygen evolution reaction: A review. *J. Energy Chem.* **2022**, *67*, 101–137. [CrossRef]

7. Jamadar, A.S.; Sutar, R.; Patil, S.; Khandekar, R.; Yadav, J.B. Progress in metal oxide-based electrocatalysts for sustainable water splitting. *Mater. Rep. Energy* **2024**, *4*, 100283. [CrossRef]

8. Li, Y.; Dong, Z.; Jiao, L. Multifunctional Transition Metal-Based Phosphides in Energy-Related. *Adv. Energy Mater.* **2020**, *10*, 1902104.

9. Hu, C.; Lv, C.; Liu, S.; Shi, Y.; Song, J.; Zhang, Z.; Cai, J.; Watanabe, A. Nickel phosphide electrocatalysts for hydrogen evolution reaction. *Catalysts* **2020**, *10*, 188. [CrossRef]

10. Sun, M.; Liu, H.; Qu, J.; Li, J. Earth-Rich Transition Metal Phosphide for Energy Conversion and Storage. *Adv. Energy Mater.* **2016**, *6*, 1600087. [CrossRef]

11. Read, C.G.; Callejas, J.F.; Holder, C.F.; Schaak, R.E. General Strategy for the Synthesis of Transition Metal Phosphide Films for Electrocatalytic Hydrogen and Oxygen Evolution. *ACS Appl. Mater. Interfaces* **2016**, *8*, 12798–12803. [CrossRef] [PubMed]

12. Zhang, H.; Li, H.; Niu, S.; Zhou, Y.; Ni, Z.; Wei, Q.; Chen, A.; Zhang, S.; Sun, T.; Dai, R.; et al. Bifunctional heterostructured nitrogen and phosphorus co-doped carbon-layer-encapsulated Co_2P electrocatalyst for efficient water splitting. *Cell Rep. Phys. Sci.* **2021**, *2*, 100586. [CrossRef]

13. Dutta, A.; Pradhan, N. Developments of Metal Phosphides as Efficient OER Precatalysts. *J. Phys. Chem. Lett.* **2017**, *8*, 144–152. [CrossRef] [PubMed]

14. Ray, A.; Sultana, S.; Paramanik, L.; Parida, K.M. Recent advances in phase, size, and morphology-oriented nanostructured nickel phosphide for overall water splitting. *J. Mater. Chem. A* **2020**, *8*, 19196–19245. [CrossRef]

15. Popczun, E.J.; McKone, J.R.; Read, C.G.; Biacchi, A.J.; Wiltrout, A.M.; Lewis, N.S.; Schaak, R.E. Nanostructured Nickel Phosphide as an Electrocatalyst for the Hydrogen Evolution Reaction. *J. Am. Chem. Soc.* **2013**, *135*, 9267–9270. [CrossRef]

16. Pan, Y.; Liu, Y.; Zhao, J.; Yang, K.; Liang, J.; Liu, D.; Hu, W.; Liu, D.; Liu, Y.; Liu, C. Monodispersed nickel phosphide nanocrystals with different phases: Synthesis, characterization and electrocatalytic properties for hydrogen evolution. *J. Mater. Chem. A* **2015**, *3*, 1656–1665. [CrossRef]

17. Lin, Y.; Pan, Y.; Zhang, J. In Situ Construction of Nickel Phosphosulfide ($Ni_5P_4 | S$) Active Species on 3D Ni Foam through Chemical Vapor Deposition for Electrochemical Hydrogen Evolution. *ChemElectroChem* **2017**, *4*, 1108–1116. [CrossRef]

18. Ramesh, S.K.; Son, J.; Ganesan, V.; Kim, J. Carbon-incorporated Ni_2P-Fe_2P hollow nanorods as superior electrocatalysts for the oxygen evolution reaction. *Nanoscale* **2022**, *136*, 16262–16269. [CrossRef] [PubMed]

19. Liao, W.; Huang, L. Improving the oxygen evolution performance of nickel phosphide nanoparticles with satellite nitrogen-doped carbon quantum dots. *Mater. Lett.* **2017**, *209*, 106–110. [CrossRef]

20. Yuan, M.; Sun, Y.; Yang, Y.; Zhang, J.; Dipazir, S.; Zhao, T.; Li, S.; Xie, Y.; Zhao, H.; Liu, Z.; et al. Boosting oxygen evolution reactivity by modulating electronic structure and honeycomb-like architecture in Ni_2P/N,P-codoped carbon hybrids. *Green Energy Environ.* **2021**, *6*, 866–874. [CrossRef]

21. Kandel, M.R.; Pan, U.N.; Dhakal, P.P.; Ghising, R.B.; Sidra, S.; Kim, D.H.; Kim, N.H.; Lee, J.H. Manganese-Doped Bimetallic $(Co,Ni)_2P$ Integrated CoP in N,S Co−Doped Carbon: Unveiling a Compatible Hybrid Electrocatalyst for Overall Water Splitting. *Small* **2024**, *20*, 2307241. [CrossRef] [PubMed]

22. Wang, B.; Liu, B.; Dai, L. Non-N-Doped Carbons as Metal-Free Electrocatalysts. *Adv. Sustain. Syst.* **2021**, *5*, 2000134. [CrossRef]

23. Zhan, X.; Tong, X.; Gu, M.; Tian, J.; Gao, Z.; Ma, L.; Xie, Y.; Chen, Z.; Ranganathan, H.; Zhang, G.; et al. Phosphorus-Doped Graphene Electrocatalysts for Oxygen Reduction Reaction. *Nanomaterials* **2022**, *12*, 1141. [CrossRef]

24. Choi, C.H.; Chung, M.W.; Kwon, H.C.; Park, S.H.; Woo, S.I. B, N- and P, N-doped graphene as highly active catalysts for oxygen reduction reactions in acidic media. *J. Mater. Chem. A* **2013**, *1*, 3694. [CrossRef]

25. Li, J.-C.; Hou, P.-X.; Cheng, M.; Liu, C.; Cheng, H.-M.; Shao, M. Carbon nanotube encapsulated in nitrogen and phosphorus co-doped carbon as a bifunctional electrocatalyst for oxygen reduction and evolution reactions. *Carbon* **2018**, *139*, 156–163. [CrossRef]

26. Choi, C.H.; Park, S.H.; Woo, S.I. Phosphorus–nitrogen dual doped carbon as an effective catalyst for oxygen reduction reaction in acidic media: Effects of the amount of P-doping on the physical and electrochemical properties of carbon. *J. Mater. Chem.* **2012**, *22*, 12107. [CrossRef]

27. Luo, S.; Wang, R.; Hei, P.; Gao, L.; Yang, J.; Jiao, T. Self-assembled Ni_2P nanosheet-implanted reduced graphene oxide composite as highly efficient electrocatalyst for oxygen evolution reaction. *Colloids Surf. A Physicochem. Eng. Asp.* **2021**, *612*, 125992. [CrossRef]

28. Ghadge, S.D.; Velikokhatnyi, O.I.; Datta, M.K.; Damodaran, K.; Shanthi, P.M.; Kumta, P.N. Highly Efficient Fluorine Doped Ni_2P Electrocatalysts for Alkaline Mediated Oxygen Evolution Reaction. *J. Electrochem. Soc.* **2021**, *168*, 064512. [CrossRef]

29. Sun, H.; Xu, X.; Yan, Z.; Chen, X.; Cheng, F.; Weiss, P.S.; Chen, J. Porous Multishelled Ni$_2$P Hollow Microspheres as an Active Electrocatalyst for Hydrogen and Oxygen Evolution. *Chem. Mater.* **2017**, *29*, 8539–8547. [CrossRef]

30. Berhault, G.; Afanasiev, P.; Loboué, H.; Geantet, C.; Cseri, T.; Pichon, C.; Guillot-Deudon, C.; Lafond, A. In Situ XRD, XAS, and Magnetic Susceptibility Study of the Reduction of Ammonium Nickel Phosphate NiNH$_4$PO$_4$·H$_2$O into Nickel Phosphide. *Inorg. Chem.* **2009**, *48*, 2985–2992. [CrossRef]

31. Rodriguez, J.A.; Kim, J.Y.; Hanson, J.C.; Sawhill, S.J.; Bussell, M.E. Physical and chemical properties of MoP, Ni$_2$P, and MoNiP hydrodesulfurization catalysts: Time-resolved X-ray diffraction, density functional, and hydrodesulfurization activity studies. *J. Phys. Chem. B* **2003**, *107*, 6276–6285. [CrossRef]

32. Zhang, Y.; Jiao, L.; Yang, W.; Xie, C.; Jiang, H.L. Rational Fabrication of Low-Coordinate Single-Atom Ni Electrocatalysts by MOFs for Highly Selective CO$_2$ Reduction. *Angew. Chem. Int. Ed.* **2021**, *60*, 7607–7611. [CrossRef] [PubMed]

33. Peng, Z.; Wang, H.; Xia, X.; Zhang, X.; Dong, Z. Integration of CoFe Alloys and Fe/Fe$_3$C Nanoparticles into N-Doped Carbon Nanosheets as Dual Catalytic Active Sites To Promote the Oxygen Electrocatalysis of Zn–Air Batteries. *ACS Sustain. Chem. Eng.* **2020**, *8*, 9009–9016. [CrossRef]

34. Artyushkova, K. Misconceptions in interpretation of nitrogen chemistry from x-ray photoelectron spectra. *J. Vac. Sci. Technol. A* **2020**, *38*, 031002. [CrossRef]

35. Luque-Centeno, J.M.; Martínez-Huerta, M.V.; Sebastián, D.; Pérez-Rodríguez, S.; Lázaro, M.J. Titanium Dioxide/N-Doped Graphene Composites as Non-Noble Bifunctional Oxygen Electrocatalysts. *Ind. Eng. Chem. Res.* **2021**, *60*, 18817–18830. [CrossRef]

36. Zhou, Z.; Wei, L.; Wang, Y.; Karahan, H.E.; Chen, Z.; Lei, Y.; Chen, X.; Zhai, S.; Liao, X.; Chen, Y. Hydrogen evolution reaction activity of nickel phosphide is highly sensitive to electrolyte pH. *J. Mater. Chem. A* **2017**, *5*, 20390–20397. [CrossRef]

37. Tiwari, A.P.; Lee, K.; Kim, K.; Kim, J.; Novak, T.G.; Jeon, S. Conformally Coated Nickel Phosphide on 3D, Ordered Nanoporous Nickel for Highly Active and Durable Hydrogen Evolution. *ACS Sustain. Chem. Eng.* **2020**, *8*, 17116–17123. [CrossRef]

38. Bernasconi, R.; Khalil, M.I.; Cakmakci, D.S.; Bektas, Y.; Nobili, L.; Magagnin, L.; Lenardi, C. Electrocatalytic layers for hydrogen evolution reaction based on nickel phosphides: Cost-effective fabrication and XPS characterization. *J. Mater. Sci.* **2022**, *57*, 9370–9388. [CrossRef]

39. Biesinger, M.C.; Payne, B.P.; Grosvenor, A.P.; Lau, L.W.M.; Gerson, A.R.; Smart, R.S.C. Resolving surface chemical states in XPS analysis of first row transition metals, oxides and hydroxides: Cr, Mn, Fe, Co and Ni. *Appl. Surf. Sci.* **2011**, *257*, 2717–2730. [CrossRef]

40. Zhang, M.; Wang, T.; Cao, H.; Cui, S.; Du, P. Self-supported Ni2P nanosheets on low-cost three-dimensional Fe foam as a novel electrocatalyst for efficient water oxidation. *J. Energy Chem.* **2020**, *42*, 71–76. [CrossRef]

41. Xiong, K.; Huang, L.; Gao, Y.; Zhang, H.; Zhuo, Y.; Shen, H.; Wang, Y.; Peng, L.; Wei, Z. Formation of a thin-layer of nickel hydroxide on nickel phosphide nanopillars for hydrogen evolution. *Electrochem. Commun.* **2018**, *92*, 9–13. [CrossRef]

42. Kumar, A.; Bui, V.Q.; Lee, J.; Jadhav, A.R.; Hwang, Y.; Kim, M.G.; Kawazoe, Y.; Lee, H. Modulating Interfacial Charge Density of NiP$_2$-FeP$_2$ via Coupling with Metallic Cu for Accelerating Alkaline Hydrogen Evolution. *ACS Energy Lett.* **2021**, *6*, 354–363. [CrossRef]

43. Kalaiyarasan, G.; Joseph, J.; Kumar, P. Phosphorus-Doped Carbon Quantum Dots as Fluorometric Probes for Iron Detection. *ACS Omega* **2020**, *5*, 22278–22288. [CrossRef]

44. Yu, Y.; Ma, J.; Chen, C.; Fu, Y.; Wang, Y.; Li, K.; Liao, Y.; Zheng, L.; Zuo, X. General Method for Synthesis Transition-Metal Phosphide/Nitrogen and Phosphide Doped Carbon Materials with Yolk-Shell Structure for Oxygen Reduction Reaction. *ChemCatChem* **2019**, *11*, 1722–1731. [CrossRef]

45. Wu, J.; Yang, Z.; Sun, Q.; Li, X.; Strasser, P.; Yang, R. Synthesis and electrocatalytic activity of phosphorus-doped carbon xerogel for oxygen reduction. *Electrochim. Acta* **2014**, *127*, 53–60. [CrossRef]

46. Sun, H.; Zhu, Y.; Yang, B.; Wang, Y.; Wu, Y.; Du, J. Template-free fabrication of nitrogen-doped hollow carbon spheres for high-performance supercapacitors based on a scalable homopolymer vesicle. *J. Mater. Chem. A* **2016**, *4*, 12088–12097. [CrossRef]

47. Wang, S.; Sun, W.; Yang, D.-S.; Yang, F. Conversion of soybean waste to sub-micron porous-hollow carbon spheres for supercapacitor via a reagent and template-free route. *Mater. Today Energy* **2019**, *13*, 50–55. [CrossRef]

48. Cui, C.M.; Guo, X.H.; Geng, Y.M.; Dang, T.T.; Xie, G.; Chen, S.P.; Zhao, F.Q. Facile one-pot synthesis of multi-yolk–shell Bi@C nanostructures by the nanoscale Kirkendall effect. *Chem. Commun.* **2015**, *51*, 9276–9279. [CrossRef]

49. Wang, Q.; Chen, S.; Shi, F.; Chen, K.; Nie, Y.; Wang, Y.; Wu, R.; Li, J.; Zhang, Y.; Ding, W.; et al. Structural Evolution of Solid Pt Nanoparticles to a Hollow PtFe Alloy with a Pt-Skin Surface via Space-Confined Pyrolysis and the Nanoscale Kirkendall Effect. *Adv. Mater.* **2016**, *28*, 10673–10678. [CrossRef]

50. Hussain, I.; Sahoo, S.; Sayed, M.S.; Ahmad, M.; Javed, M.S.; Lamiel, C.; Li, Y.; Shim, J.J.; Ma, X.; Zhang, K. Hollow nano- and microstructures: Mechanism, composition, applications, and factors affecting morphology and performance. *Coord. Chem. Rev.* **2022**, *458*, 214429. [CrossRef]

51. Cho, J.S.; Won, J.M.; Lee, J.-H.; Kang, Y.C. Synthesis and electrochemical properties of spherical and hollow-structured NiO aggregates created by combining the Kirkendall effect and Ostwald ripening. *Nanoscale* **2015**, *7*, 19620–19626. [CrossRef]

52. Xie, X.; Shang, L.; Shi, R.; Waterhouse, G.I.N.; Zhao, J.; Zhang, T. Tubular assemblies of N-doped carbon nanotubes loaded with NiFe alloy nanoparticles as efficient bifunctional catalysts for rechargeable zinc-air batteries. *Nanoscale* **2020**, *12*, 13129–13136. [CrossRef] [PubMed]

53. Diaz-Morales, O.; Ferrus-Suspedra, D.; Koper, M.T.M. The importance of nickel oxyhydroxide deprotonation on its activity towards electrochemical water oxidation. *Chem. Sci.* **2016**, *7*, 2639–2645. [CrossRef]

54. Stern, L.A.; Feng, L.; Song, F.; Hu, X. Ni$_2$P as a Janus catalyst for water splitting: The oxygen evolution activity of Ni$_2$P nanoparticles. *Energy Environ. Sci.* **2015**, *8*, 2347–2351. [CrossRef]

55. Wu, Z.; Vagin, M.; Boyd, R.; Bakhit, B.; Greczynski, G.; Odén, M.; Björk, E.M. Morphology effects on electrocatalysis of anodic water splitting on nickel (II) oxide. *Microporous Mesoporous Mater.* **2022**, *333*, 111734. [CrossRef]

56. Lyons, M.E.G.; Brandon, M.P. The significance of electrochemical impedance spectra recorded during active oxygen evolution for oxide covered Ni, Co and Fe electrodes in alkaline solution. *J. Electroanal. Chem.* **2009**, *631*, 62–70. [CrossRef]

57. Wang, Q.; Liu, Z.; Zhao, H.; Huang, H.; Jiao, H.; Du, Y. MOF-derived porous Ni$_2$P nanosheets as novel bifunctional electrocatalysts for the hydrogen and oxygen evolution reactions. *J. Mater. Chem. A* **2018**, *6*, 18720–18727. [CrossRef]

58. Wang, M.; Lin, M.; Li, J.; Huang, L.; Zhuang, Z.; Lin, C.; Zhou, L.; Mai, L. Metal–organic framework derived carbon-confined Ni$_2$P nanocrystals supported on graphene for an efficient oxygen evolution reaction. *Chem. Commun.* **2017**, *53*, 8372–8375. [CrossRef]

59. Li, R.; Wei, Z.; Gou, X. Nitrogen and Phosphorus Dual-Doped Graphene/Carbon Nanosheets as Bifunctional Electrocatalysts for Oxygen Reduction and Evolution. *ACS Catal.* **2015**, *5*, 4133–4142. [CrossRef]

60. Li, J.; Tian, Q.; Jiang, S.; Zhang, Y.; Wu, Y. Electrocatalytic performances of phosphorus doped carbon supported Pd towards formic acid oxidation. *Electrochim. Acta* **2016**, *213*, 21–30. [CrossRef]

61. McCrory, C.C.L.; Jung, S.; Peters, J.C.; Jaramillo, T.F. Benchmarking Heterogeneous Electrocatalysts for the Oxygen Evolution Reaction. *J. Am. Chem. Soc.* **2013**, *135*, 16977–16987. [CrossRef] [PubMed]

62. Zhao, X.; Chen, X.; Wang, Y.; Song, P.; Zhang, Y. High-efficiency Ni–P catalysts in amorphous and crystalline states for the hydrogen evolution reaction. *Sustain. Energy Fuels* **2020**, *4*, 4733–4742. [CrossRef]

63. Zhang, X.; Ma, G.; Shui, L.; Zhou, G.; Wang, X. Urea electrooxidation-boosted hydrogen production on nitrogen-doped porous carbon nanorod-supported nickel phosphide nanoparticles. *J. Energy Chem.* **2022**, *72*, 88–96. [CrossRef]

64. Mijowska, E.; Pietrusewicz, K.; Maślana, K. Highly Porous Carbon Flakes Derived from Cellulose and Nickel Phosphide Heterostructure towards Efficient Electrocatalysis of Oxygen Evolution Reaction. *Molecules* **2024**, *29*, 352. [CrossRef]

65. Yan, L.; Jiang, H.; Wang, Y.; Li, L.; Gu, X.; Dai, P.; Liu, D.; Tang, S.F.; Zhao, G.; Zhao, X.; et al. One-step and scalable synthesis of Ni$_2$P nanocrystals encapsulated in N,P-codoped hierarchically porous carbon matrix using a bipyridine and phosphonate linked nickel metal–organic framework as highly efficient electrocatalysts for overall water splitting. *Electrochim. Acta* **2019**, *297*, 755–766. [CrossRef]

66. Cebollada, J.; Sebastián, D.; Lázaro, M.J.; Martínez-Huerta, M.V. Carbonized Polydopamine-Based Nanocomposites: The Effect of Transition Metals on the Oxygen Electrocatalytic Activity. *Nanomaterials* **2023**, *13*, 1549. [CrossRef]

67. Dent, A.J.; Cibin, G.; Ramos, S.; Smith, A.D.; Scott, S.M.; Varandas, L.; Pearson, M.R.; Krumpa, N.A.; Jones, C.P.; Robbins, P.E. B18: A core XAS spectroscopy beamline for Diamond. *J. Phys. Conf. Ser.* **2009**, *190*, 012039. [CrossRef]

68. Ravel, B.; Newville, M. ATHENA, ARTEMIS, HEPHAESTUS: Data analysis for X-ray absorption spectroscopy using IFEFFIT. *J. Synchrotron Radiat.* **2005**, *12*, 537–541. [CrossRef]

69. Li, J.; Li, J.; Zhou, X.; Xia, Z.; Gao, W.; Ma, Y.; Qu, Y. Highly Efficient and Robust Nickel Phosphides as Bifunctional Electrocatalysts for Overall Water-Splitting. *ACS Appl. Mater. Interfaces* **2016**, *8*, 10826–10834. [CrossRef]

70. Ji, X.; Lin, Y.; Zeng, J.; Ren, Z.; Lin, Z.; Mu, Y.; Qiu, Y.; Yu, J. Graphene/MoS2/FeCoNi(OH)x and Graphene/MoS2/FeCoNiPx multilayer-stacked vertical nanosheets on carbon fibers for highly efficient overall water splitting. *Nat. Commun.* **2021**, *12*, 1380. [CrossRef]

71. Kumar, P.; Murthy, A.P.; Bezerra, L.S.; Martini, B.K.; Maia, G.; Madhavan, J. Carbon supported nickel phosphide as efficient electrocatalyst for hydrogen and oxygen evolution reactions. *Int. J. Hydrogen Energy* **2021**, *46*, 622–632. [CrossRef]

72. Bhanja, P.; Kim, Y.; Paul, B.; Kaneti, Y.V.; Alothman, A.A.; Bhaumik, A.; Yamauchi, Y. Microporous nickel phosphonate derived heteroatom doped nickel oxide and nickel phosphide: Efficient electrocatalysts for oxygen evolution reaction. *Chem. Eng. J.* **2021**, *405*, 126803. [CrossRef]

73. Battiato, S.; Urso, M.; Cosentino, S.; Pellegrino, A.L.; Mirabella, S.; Terrasi, A. Optimization of Oxygen Evolution Reaction with Electroless Deposited Ni–P Catalytic Nanocoating. *Nanomaterials* **2021**, *11*, 3010. [CrossRef] [PubMed]

74. Louie, M.W.; Bell, A.T. An Investigation of Thin-Film Ni–Fe Oxide Catalysts for the Electrochemical Evolution of Oxygen. *J. Am. Chem. Soc.* **2013**, *135*, 12329–12337. [CrossRef]

75. Cheng, N.; Liu, Q.; Tian, J.; Sun, X.; He, Y.; Zhai, S.; Asiri, A.M. Nickel oxide nanosheets array grown on carbon cloth as a high-performance three-dimensional oxygen evolution electrode. *Int. J. Hydrogen Energy* **2015**, *40*, 9866–9871. [CrossRef]

76. Li, Z.; Dou, X.; Zhao, Y.; Wu, C. Enhanced oxygen evolution reaction of metallic nickel phosphide nanosheets by surface modification. *Inorg. Chem. Front.* **2016**, *3*, 1021–1027. [CrossRef]

77. Hung, K.-M.; Wu, J.-J. Bifunctional nickel phosphide nanoparticle/nickel cobalt sulfide nanosheet framework for electrocatalytic simultaneous hydrogen evolution and 2,5-Furandicaroxylic acid production. *Chem. Eng. J.* **2024**, *484*, 149772. [CrossRef]